

Electro-chemo-mechanical simulation for lithium ion batteries across the scales

Tobias Hofmann^a, Daniel Westhoff^b, Julian Feinauer^b, Heiko Andrä^a, Jochen Zausch^a, Volker Schmidt^b, Ralf Müller^c

^a*Fraunhofer ITWM, Kaiserslautern, Department of Flow and Materials simulation*

^b*Ulm University, Institute of Stochastics*

^c*University of Kaiserslautern, Institute of Applied Mechanics*

Abstract

In this work a phase field method is used for the solution of an electro-chemical diffusion model for a lithium-iron-phosphate particle coupled to a small-strain elasto-plasticity model. This coupling takes the mechanical dilatation of the crystal lattice during intercalation into account. The electro-chemo-mechanical coupling is derived from a Helmholtz free energy, resulting in constitutive equations for both the diffusion and the mechanical equilibrium in the electrode material. A new method for the generation of virtual microstructures is given with additional constraints to obtain smooth boundaries. This ensures valid mechanical solutions for grid refinement. The model is then discretized, linearized and solved for various microstructures. Academic results in one and two spatial dimensions are presented as well as results on spherical structures. The versatility of the numerical method is demonstrated for virtual microstructures generated by stochastic models on graphite.

1. Introduction

A lot of electrode materials for lithium ion batteries show capacity fade or degradation phenomena during their lifetime. Large discharge currents result in steep concentration gradients due to slow lithium ion diffusion. High gradients of lithium ion concentration result in high mechanical stresses due to the local dilatation of the particles. Those contribute to the aging of the whole battery

cell.

Different materials have been used as electrolyte as well as for the cathode and the anode. In a lot of them, the electrochemical processes can be accurately described by Fickian diffusion for the lithium ion concentration field and the Gaussian law for the electric potential field. But especially in the popular cathode material lithium-iron-phosphate (LiFePO_4 , LFP), the diffusion of the lithium ions from the electrolyte into the active material cannot be modelled by a regular diffusion equation. In a lot of materials the diffusion leads to a uniform ion distribution inside the material. But in lithium-iron-phosphate the lithium ions separate into areas with a maximum concentration of lithium ions and areas where no lithium ions are present [1, 2, 3, 4]. Even without applied current, the lithium rich areas do not diffuse. The distribution of the lithium ions inside the material can then be described by two different phases, one phase rich with lithium ions and one phase depleted of lithium ions. The process of separation into different phases is called spinodal decomposition. The problem of describing the movement of the boundaries between both phases is often referred to as Stefan problem [5, 6] and can be approached by adaptive meshes and front-tracking methods [7].

Another approach called phase-field method is introduced in the works by Cahn and Hilliard [8] and is based on a thermodynamical approach involving a non-convex Helmholtz energy functional. In a general phase-field method, the interface between two phases is regularized [9]. Phase-field methods have been applied for the solution of displacive problems such as the phase transformation between austenite and martensite [10, 11] or mechanical fracture processes [12, 13].

In phase-field models for diffusive processes, the governing fourth-order non-linear partial differential equation is called the Cahn-Hilliard equation. Recent formulations for lithium-iron-phosphate particles can be found in [14, 15, 16, 17, 18]. While those models are restricted to simulations of electrode material, the model presented in this paper describes diffusion and electric potentials in both electrodes and the electrolyte. There are simulations for the charging of elec-

trode material for different spherical [19, 20], ellipsoidal nanoparticles [21, 22] or more complex single particle microstructures [23, 24, 25]. The effects of charging on porous electrodes has also been studied [26, 27, 28, 29, 30]. Instead of the resolution of a microstructure, homogenization is often applied [26, 31].

If one however wants to consider the entire 3D structural information, stochastic microstructure models are a powerful tool to generate a broad spectrum of realistic 3D input data. These models are based on methods of stochastic geometry [32] and can be constructed for very different materials like organic solar cells [33], open-cell foams [34], SOFC-electrodes [35] and battery electrodes [36]. Once calibrated using tomographic image data of real microstructures, model parameters can be varied systematically to generate a broad spectrum of virtual microstructures. Using, e.g., numerical transport simulations, this data basis can be used to investigate the relationships between descriptors of the 3D morphology and functionality of the materials [37].

In Section 2, an electro-chemo-mechanical model for the simulation of a lithium ion battery on the microscale is given. The model is valid for a porous microstructure of electrode domain. This microstructure may be given by computer tomography and image segmentation. It is also possible to design virtual microstructures using stochastic models. The intercalation of the lithium ions into the electrode material is modelled by Butler-Volmer kinetics. The transport of lithium ions inside the electrode material is described by the Cahn-Hilliard diffusion equation, while the mechanical dilatation of the electrode material is caused by a chemical strain which is proportional to the local lithium ion concentration. Usually the diffusive properties of lithium-iron phosphate are modelled by a free energy that depends on the logarithm of the concentration. Those are difficult to solve efficiently. In this work, the energy is approximated by a polynomial of fourth order with optimal coefficients. For these polynomials, efficient methods have been developed.

In Section 3, a method for the generation of three-dimensional microstructures with smooth Lipschitz boundaries is given. The main volume of the electrode material is approximated in the shape of regular spherical grids. Then

binder material is added by two different methods such that the domain boundary is Lipschitz¹. The resulting elastic problem is solved for a constant concentration and shown to be stable for grid refinement. Afterwards, the numerical method for the electro-chemical problem is shortly introduced similar to [38]. Next, a numerical application is given. First the elastic effects are investigated with the help of academic examples. The mechanical stress affects the equilibrium concentration in lithium-rich and lithium-depleted phase as well as the cell voltage.

In Section 4, realistic 3D microstructures are considered, which have been generated using stochastic microstructure models. In [39], a first approach how to combine electro-chemo-mechanical simulations with 3D microstructure modeling has been proposed, which is extended in the present paper. To begin with, we compare tomographic image data with realizations of a calibrated stochastic microstructure model [40]. After that, virtual microstructures are considered for systematic ally varied volume fractions of active material. These structures have been generated using the method described in [41].

In Section 5, a short summary of the obtained results is given and future steps for the further development are discussed.

2. Electro-chemo-mechanical model

In this section, the equations for a lithium ion battery model on the microscale are presented. The mathematical model involves the fields of the concentration c , the electric potential ϕ , the chemical potential μ , and the vector field displacement \mathbf{u} . The movement of electrons and the charging of a battery is related to the local concentration c and diffusion of positive lithium ions Li^+ . The electric potential ϕ is connected to the current provided by the battery during usage. The lithium ion intercalation into electrode material results in

¹Lipschitz domains may include corners, i.e. a non-smooth domain boundary. The presented method additionally guarantees C^1 -continuity of the boundary.

Name	Symbol	Unit
Concentration	c	mol cm^{-3}
Displacement	\mathbf{u}	cm
Lithium ion flux	f_{se}	$\text{mol cm}^{-2} \text{s}^{-1}$
Strain	ε	1
Stress	$\boldsymbol{\sigma}$	GPa

Table 1: Definition of symbols and constants.

the local displacement \mathbf{u} of the electrodes. In Table 1, symbols and units are defined.

In a cuboid domain $\Lambda = (0, L_1) \times (0, L_2) \times (0, L_3) \subset \mathbb{R}^3$ the microstructure of a solid battery electrode Ω is embedded. The particle boundary of Ω is denoted by $\Gamma = \partial\Omega$. Given the time interval $T = (0, t_0)$, a time-dependent problem is posed on $\Omega \times T$.

Partial differential equations for the concentration field $c(\mathbf{x}, t)$ and the displacement $\mathbf{u}(\mathbf{x}, t)$ will be defined. The boundary conditions will be given by the Butler-Volmer flux relation $f_{se}(\mathbf{x}, t)$ on $\Gamma \times T$. In this context, the trace operator γ_0 is introduced that gives the trace of a scalar field defined on Ω onto Γ ,

$$\gamma_0 : c(\mathbf{x}, t) \mapsto c_\gamma(\mathbf{x}, t) = \lim_{\Omega \ni \tilde{\mathbf{x}} \rightarrow \mathbf{x} \in \Gamma} c(\tilde{\mathbf{x}}, t). \quad (1)$$

2.1. Thermodynamical modeling

A phase-field model for the concentration $c(\mathbf{x}, t)$ is considered. The phase-field parameter is here the normalized lithium ion concentration $p = \frac{c(\mathbf{x}, t)}{c_{\max}}$. Motivated by previous works in [16, 42, 21], the free energy is assumed as

$$E_{\log}(p) = RT \left(p \log(p) + (1-p) \log(1-p) + \frac{q}{RT} p(1-p) \right) + \frac{1}{2} \varepsilon_{\text{el}} : \mathbb{C} : \varepsilon_{\text{el}} + E_{\text{plas}}, \quad (2)$$

with the mixing enthalpy q , the gas constant R and the temperature T given in Table 2. Electric contributions to the energy are not considered. By not including all terms into the free energy, the problem is simplified and the application

of the Cahn-Hilliard scheme does not describe a whole system entirely. The full theoretical approach is still an open problem and not given in this work.

The first term is related to a diffusion potential based on one-body terms in a Hamiltonian of the crystalline structure in active material. The second term results from a mean-field approximation of two-body interaction terms in the Hamiltonian. The equilibrium values for p are given by the minimizers of $E'_{\log}(p) = 0$ as p_1 and p_2 .

2.2. Electro-chemical model

Transport equations in the electrolyte domain, the anode domain, and the cathode domain are introduced separately based on [44]. The transport equations for ion concentration c_e and the electric potential ϕ_e in a liquid electrolyte are considered as

$$\partial_t c_e = \partial_t c_e = \nabla \cdot \left[\left(D_e + \frac{\kappa_e R T t_+ (t_+ - 1)}{F^2 c_e} \right) \nabla c_e + \frac{\kappa_e t_+}{F} \nabla \phi_e \right], \quad (3a)$$

$$0 = \nabla \cdot \left[\kappa_e \frac{(t_+ - 1)}{F c_e} \nabla c_e + \kappa_e \nabla \phi_e \right]. \quad (3b)$$

Here constants R , T and F are the universal gas constant, the temperature, and the Faraday constant, respectively. The electro-chemical properties of the electrolyte are given by its diffusivity D_e and its conductivity κ_e . Depending on the transference number t_+ , the transport of positive lithium ions is coupled to the transport of additional negative anions. The units fit the following way. First look at the dimensions of the following expression,

$$\left[\frac{\kappa_e R T t_+ (t_+ - 1)}{F^2 c_e} \right] = \frac{\frac{\text{A}}{\text{V cm}} \frac{\text{J}}{\text{mol K}} \text{K}}{\left(\frac{\text{A s}}{\text{mol}} \right)^2 \frac{\text{mol}}{\text{cm}^3}} = \frac{\frac{\text{A J}}{\text{V cm mol}}}{\frac{\text{A}^2 \text{s}^2}{\text{mol cm}^3}} = \frac{\frac{\text{J}}{\text{V}}}{\frac{\text{A s}^2}{\text{cm}^2}} = \frac{\frac{\text{V A s}}{\text{V}}}{\frac{\text{A s}^2}{\text{cm}^2}} = \frac{\text{cm}^2}{\text{s}}, \quad (4)$$

which is the same dimension as the diffusion coefficient. The expression $D_e \nabla c_e$ then has the unit $\text{mol s}^{-1} \text{cm}^{-2}$, which is the same as the second term inside the square brackets in 3a,

$$\left[\frac{\kappa_e t_+}{F} \nabla \phi_e \right] = \frac{\frac{\text{A}}{\text{V cm}}}{\frac{\text{A s}}{\text{mol}}} \frac{1}{\text{cm}} \text{V} = \frac{\text{mol}}{\text{s cm}^2}. \quad (5)$$

Name	Symbol	Value	Unit
Universal gas constant	R	8.314	$\text{J mol}^{-1} \text{K}^{-1}$
Temperature	T	300	K
Faraday constant	F	96485	A s mol^{-1}
Diffusivity	D	10^{-10}	$\text{cm}^2 \text{s}^{-1}$
Max. Li-ion conc.	c_{\max}	0.02	mol cm^{-3}
Young's modulus	E	125	GPa
Poisson's ratio	ν	0.3	-
Partial molar vol.	θ	3.497	$\text{cm}^3 \text{mol}^{-1}$
Mixing enthalpy	q	$1.110 \cdot 10^4$	J mol^{-1}
Kappa	κ	$2.508 \cdot 10^{-10}$	$\text{J cm}^2 \text{mol}^{-1}$
Rate constant	k	$3.159 \cdot 10^{-8}$	$\text{mol cm}^{-2} \text{s}^{-1}$
Young's modulus (silicon)	E	160	GPa
Hardening parameters (silicon)	σ^0	0.4	GPa
	σ^∞	0.6	GPa
	H^0	1.0	GPa
	H^∞	0.1	GPa
Young's modulus (graphite)	E	109	GPa

Table 2: Material parameters partially taken from [43, 44, 42, 45, 46]. Parameters for silicon taken from [47, 48].

The equation 3a can be derived from Equations 23 and 50 in [44]. Given a chemical potential for the electrolyte $\mu_e = RT \log(c)$, setting the charge constant z_+ to 1 because we consider lithium ions, and disregarding temperature gradients, the Equation 23 is then

$$\mathbf{j} = -\kappa \nabla \phi - \kappa \frac{t_+ - 1}{F} \frac{RT}{c} \nabla c. \quad (6)$$

This can be plugged into Equation 50 in [44], which gives

$$\begin{aligned} \partial_t c_e &= \nabla \cdot [D_e \nabla c_e] - \nabla \cdot \left[\frac{t_+}{F} \mathbf{j} \right] \\ &= \nabla \cdot [D_e \nabla c_e] - \nabla \cdot \left[-\frac{t_+ \kappa}{F} \nabla \phi - \frac{\kappa t_+ (t_+ - 1) RT}{F^2 c} \nabla c \right] \\ &= \nabla \cdot \left[D_e \nabla c_e + \frac{t_+ \kappa}{F} \nabla \phi + \frac{\kappa t_+ (t_+ - 1) RT}{F^2 c} \nabla c \right] \\ &= \nabla \cdot \left[D_e \nabla c_e + \frac{t_+ \kappa}{F} \nabla \phi + \frac{\kappa t_+ (t_+ - 1) RT}{F^2 c} \nabla c \right] \\ &= \nabla \cdot \left[\left(D_e + \frac{\kappa t_+ (t_+ - 1) RT}{F^2 c} \right) \nabla c + \frac{t_+ \kappa}{F} \nabla \phi \right], \end{aligned} \quad (7)$$

which is Equation 3a. Inside the electrode material, the lithium ion diffusion c_s and the electric potential ϕ_s are decoupled by the equations

$$\partial_t c_s = \nabla \cdot \left[\frac{D_s}{RT} \nabla c_s \right], \quad (8a)$$

$$0 = \nabla \cdot [\kappa_s \nabla \phi_s], \quad (8b)$$

where D_s denotes the corresponding diffusivity, and κ_s the conductivity.

2.3. Cahn-Hilliard equation

For a numerically efficient solution E_{\log} is replaced by a polynomial approximation

$$E_{\text{poly}}(p) = a_0 \left(p - \frac{1}{2} \right)^4 + a_1 \left(p - \frac{1}{2} \right)^2 + a_2, \quad (9)$$

with $a_0, a_1, a_2 \in \mathbb{R}$ chosen as appropriate fit parameters. By definition it is symmetric around $p = 0.5$. Three conditions ensuring existence and uniqueness are given by

- $E'_{\text{poly}}(p_i) = 0, i \in \{1, 2\}$,

p_1	p_2	a_0	a_1	a_2
0.0129	0.9871	7.667	-3.638	0.419

Table 3: Parameters for the polynomial fit

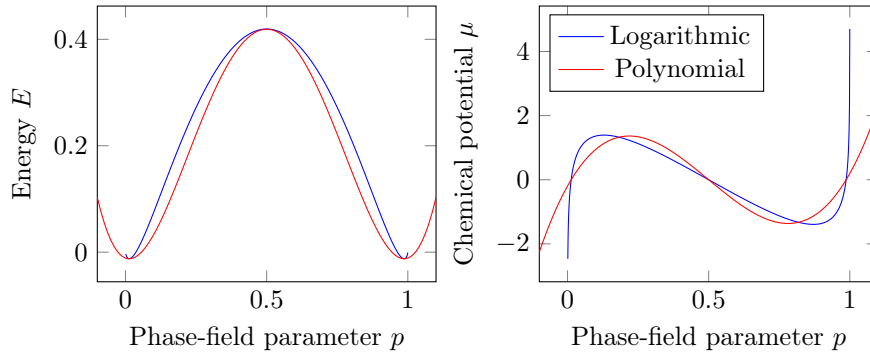


Figure 1: Energy (a) and chemical potential (b) for logarithmic and polynomial approximation.

- $E_{\text{poly}}(p_i) = E_{\text{log}}(p_i)$, $i \in \{1, 2\}$,
- $E_{\text{poly}}(\frac{1}{2}) = E_{\text{log}}(\frac{1}{2})$.

The first condition ensures that the equilibrium concentrations are the same as for the logarithmic potential. The second condition ensures that the energy content of the equilibrium concentration is preserved. The last condition ensures that the activation energy² remains unaltered. The resulting parameters of the polynomial approximation are given in Table 3. In Figure 1, the logarithmic energy and the polynomial fit are compared to each other as well as the derivative, the chemical potential. The phase interface between lithium-rich phase and lithium-depleted phase is related to misfits in the crystal structure. Therefore, a penalty term involving a norm of the gradient of the phase-field parameter is added to the free energy

$$E(p) = E_{\text{poly}}(p) + \frac{\kappa}{2RT} |\nabla p|^2. \quad (10)$$

²Maximum height of the energy landscape between equilibrium concentrations.

The chemical potential is then defined as the variational derivative,

$$\begin{aligned} \mu(\mathbf{x}, t) &= \frac{\delta E}{\delta p} = \partial_p E(p) - \nabla \partial_{\nabla p} E(p) = \\ &4a_0 \left(p(\mathbf{x}, t) - \frac{1}{2} \right)^3 + 2a_1 \left(p(\mathbf{x}, t) - \frac{1}{2} \right) - \frac{\kappa}{RT} \Delta p(\mathbf{x}, t), \end{aligned} \quad (11)$$

and coupled to the diffusion equation by

$$\partial_t c(\mathbf{x}, t) = \text{div} \left(Dc(\mathbf{x}, t) \left(1 - \frac{c(\mathbf{x}, t)}{c_{\max}} \right) \nabla \mu(\mathbf{x}, t) \right). \quad (12)$$

Here the diffusion coefficient is approximated at $c = \frac{c_{\max}}{2}$. By this (12) is now linear in the chemical potential. The equation is then rewritten in terms of the time evolution of the non-dimensional phase-field parameter, yielding

$$\partial_t p(\mathbf{x}, t) = \frac{D}{4} \Delta \mu(\mathbf{x}, t). \quad (13)$$

By combining (11) and (13) the Cahn-Hilliard equation is obtained,

$$\partial_t p(\mathbf{x}, t) = \frac{D}{4} \Delta \left(4a_0 \left(p(\mathbf{x}, t) - \frac{1}{2} \right)^3 + 2a_1 \left(p(\mathbf{x}, t) - \frac{1}{2} \right) + \frac{\kappa}{RT} \Delta p(\mathbf{x}, t) \right). \quad (14)$$

This equation may look unusual to some readers comparing to the known classical equation in e.g. [49], there given as Eq. 4.15,

$$\frac{\partial \phi}{\partial t} = M \nabla^2 \left(-W_a \nabla^2 \phi + a_2 \phi + a_4 \phi^3 \right) \quad (15)$$

Now, this equation can be compared to ours by replacing the ϕ with the variable p , the ∇^2 with the letter Δ , as well as other names for the numeric coefficients. Please also note the similar polynomial dependence of third order, only differing in numerical coefficients.

2.4. Mechanical model

The strain in the material is decomposed into a chemical, an elastic and a plastical part as

$$\boldsymbol{\varepsilon} = \boldsymbol{\varepsilon}_{\text{ch}} + \boldsymbol{\varepsilon}_{\text{el}} + \boldsymbol{\varepsilon}_{\text{pl}} = \frac{\theta c}{3} \mathbf{I} + \boldsymbol{\varepsilon}_{\text{el}} + \boldsymbol{\varepsilon}_{\text{pl}}. \quad (16)$$

The first component, the chemical strain is locally different due to different local concentrations. By this way, concentration gradients result in different local expansion of the particle. The chemical strain is assumed as a hydrostatic dilatation depending on the partial molar volume coefficient θ . The constitutive equation for the stress is then given as the variational derivative of the free energy in (2) as

$$\boldsymbol{\sigma} = \mathbb{C} : \boldsymbol{\varepsilon}_{\text{el}} = \mathbb{C} : \left(\boldsymbol{\varepsilon} - \frac{\theta c}{3} \mathbf{I} - \boldsymbol{\varepsilon}_{\text{pl}} \right) \quad (17)$$

In the simulation on the lithium-iron-phosphate on the nano-scale, the plastic strain will be disregarded. Assuming a linear elastic isotropic material behavior with the two Lamé constants λ and μ , the set of mechanical field equations is given by

$$\begin{aligned} \boldsymbol{\varepsilon}_{\text{el}} &= \frac{1}{2}(\nabla \mathbf{u} + \nabla \mathbf{u}^T) - \frac{\theta}{3} c \mathbf{I}, \\ \boldsymbol{\sigma} &= \lambda \text{Tr}(\boldsymbol{\varepsilon}_{\text{el}}) \mathbf{I} + 2\mu \boldsymbol{\varepsilon}_{\text{el}}, \\ 0 &= \text{div } \boldsymbol{\sigma}. \end{aligned} \quad (18)$$

Concerning its mechanical behavior, the electrolyte region $\Lambda \setminus \Omega$ is assumed to behave like pore space. The dilatation due to intercalation of the particle displaces the electrolyte.

2.5. Extension to rate-independent small strain elasto-plasticity

Mechanical modeling of electrode microstructures has also been extended to include plasticity [50, 51, 52, 22, 53]. The model presented in this section is able to characterize permanent changes to the battery microstructure. For the sake of simplicity, we consider von Mises J_2 plasticity with isotropic hardening [54, 55, 56]. First we introduce one scalar internal variable r as isotropic hardening parameter. The expansion of the yield surface by isotropic hardening is characterized by the yield function

$$\sigma_y(r) = \sigma^0 + H^0 r + (\sigma^\infty - \sigma^0) [1 - \exp(-\delta r),]$$

for given material parameters $\sigma^\infty \geq \sigma^0 \geq 0, H^\infty \geq H^0 \geq 0$ and

$$\delta = \frac{H^\infty - h^0}{\sigma^\infty - \sigma^0}.$$

Now we construct the plastic energy contribution and the plastic evolution such that the classic yield condition is satisfied. By decomposition of the free energy into elastic and plastic part, and introduction of the conjugate internal variable R , a constitutive relation is defined. Following this the evolution of the internal variables is derived from the plastic dissipation potential. The presented model does not take kinematic hardening and viscous effects into account, i.e. a quasistatic problem is solved.

2.6. Interface, boundary and initial conditions

For the formulation of interface conditions, a simplified and modified Butler-Volmer equation is used where reversible processes are not taken into account. The Butler-Volmer flux i_{se} [44] is defined similar to other work [57, 58, 59, 60] as

$$i_{se} = k \sqrt{c_e c_s (c_{s,max} - c_s)} \sinh \left(\frac{F}{2RT} (\phi_s - U_0) \right). \quad (19)$$

where k is the Butler-Volmer rate constant and ϕ_s is the spatially constant electric potential inside the particle using equations 34, 39 and 40 from [44]. Following are the direct quotes of those equations from [44]. Equation 34 in [44] is

$$i_{se} = i_0 \left(\exp \left[\frac{\alpha_a F}{RT} \eta_s \right] - \exp \left[\frac{-\alpha_c F}{RT} \eta_s \right] \right), \quad (20)$$

where i_0 is called exchange current density, α_A and α_C are weighting the anodic and the cathodic contribution of the overpotential η_s to the overall reaction. The overpotential is the deviation of the electrochemical potential from the chemical equilibrium between active particle and electrolyte. By detailed derivation which is not reproduced here, it can be derived as Equation 39 in [44],

$$\eta_s = \phi_s - \phi_e - U_0. \quad (21)$$

The variable ϕ_e is here the electrochemical potential instead of the electric potential. The amplitude of the exchange current density i_0 in Equation 20 is given in Equation 40 in [44] as

$$i_0 = k c_e^{\alpha_a} c_s^{\alpha_a} (c_{s,max} - c_s)^{\alpha_c}, \quad (22)$$

where k is a reaction rate and $c_{s,max}$ is the maximum concentration of ions in the active particle. Now assuming that $\alpha_a = \alpha_c = 0.5$, the Equations 20, 21, and 22 can be simplified to the presented form in Equation 19. The electric potential of the surrounding electrolyte is here assumed as constant zero. The value

$$\eta = \frac{F}{2RT} \phi(t) - U(c(\mathbf{x}, t)) \quad (23)$$

is called overpotential. The assumptions of locally constant electric potentials are valid for small structures in the range of microns and due to the high conductivity of the regarded material. The hyperbolic function is a result of the approximation of chemical reaction rates. The open circuit potential $U(c)$ is given as a function from measurements, see Figure 2. The concentration flux is used to define a Neumann boundary condition,

$$\mathbf{n} \cdot \left(\frac{D}{4} \nabla \mu(\mathbf{x}, t) \right) = f(\mathbf{x}, t) \quad \text{for all } \mathbf{x} \in \Gamma. \quad (24)$$

With the electric solid potential ϕ as an additional scalar degree of freedom, another equation is required to close the system. For this, the parameter C-rate is introduced to define a meaningful charging boundary condition. It is defined as the quotient of the constant volume flux into the battery and the maximum

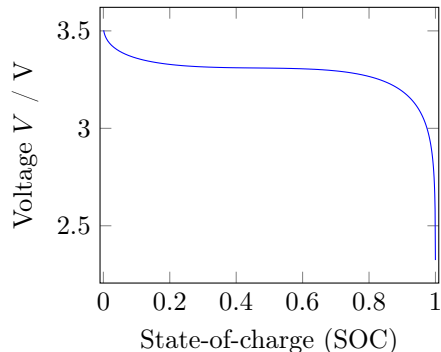


Figure 2: Open circuit potential of lithium-iron-phosphate [61].

lithium ion capacity of the battery. It is usually specified in the unit h^{-1} . A given rate C then defines a concentration flux F such that it takes $\frac{1}{C}$ hours to charge the battery cell from empty to full state of charge,

$$F = \frac{|\Omega|}{|\Gamma|} C. \quad (25)$$

This puts an integral condition on the concentration flux f as

$$\frac{1}{|\Gamma|} \int_{\Gamma} f(\mathbf{x}, t) = \frac{|\Omega|}{|\Gamma|} C, \quad \text{for all } t \in T, \quad (26)$$

that can be used to calculate $\phi(t)$. In this paper, active solid material as well as binder and conductive additives are not considered separately on the continuum scale. This is reflected in the material coefficients, e.g. the maximum concentration of the active material. For the chemical potential $\mu(\mathbf{x}, t)$, an additional boundary condition along Γ is needed, called surface wetting. The applied boundary condition corresponds to neither strong wetting nor strong dewetting,

$$\mathbf{n} \cdot \nabla c = 0, \quad (\mathbf{x}, t) \in \Gamma \times T. \quad (27)$$

As the microstructure is assumed to be periodic, periodic boundary conditions are chosen for the mechanical model. The microstructure is interpreted as a representative volume element and no macroscopic displacements are assumed. Therefore, the displacements are periodic and identical on opposite sites. The

boundary conditions are then

$$\mathbf{u}(\mathbf{x}, t) = \mathbf{u}(\mathbf{x} + L_i \mathbf{e}_i, t), \quad (\mathbf{x}, t), (\mathbf{x} + L_i \mathbf{e}_i, t) \in \partial\Lambda \times T, i \in \{1, 2, 3\}. \quad (28)$$

Because the electrolyte is modeled as pore material, it is displaced by the expanding electrode material. Therefore on the particle boundary Γ , a traction free condition is fulfilled as

$$\boldsymbol{\sigma}(\mathbf{x}, t) \cdot \mathbf{n} = 0, \quad \text{for all } (\mathbf{x}, t) \in \Gamma \times T. \quad (29)$$

The simulation of the charging of a microstructure is initialized with a constant concentration

$$(30)$$

$c_0 \in \mathbb{R}^+$. This is a static equilibrium state as no concentration gradient is present. It corresponds to a state of charge $\text{SOC} = \frac{c_0}{c_{\max}}$. It is possible to calculate consistent initial values for the concentration flux $f(\mathbf{x}, 0) = f_0$ and the electric solid potential $\phi(0) = \phi_0$, which solve the respective governing static Equations (19) and (26). The open circuit potentials for graphite and silicon are taken from [62, 63].

3. Application on the nano-scale: Cathode made of LFP

In this section, an application on the nano-scale for the material lithium-iron phosphate is given. First an algorithm for the generation and extension of periodic microstructures is introduced. Spherical packings are introduced in Section 3.1 and an elastic test is presented. Regular spherical packings inspired by atomic lattices are considered. Those regular structures are only used in order to enable the study of interactions of different contacting particles. They are not supposed to represent real arrangements of perfect spherical particles on the nanoscale. The concept of regularisation is introduced in Section 3.2. Then two different coating methods are analyzed in Section 3.3 and Section 3.4 and compared in Section 3.5. The elastic test example is repeated with the regularised microstructures in Section 3.6. In Section 3.7, basic results for the

charging of a spherical particle are given. The phase separation is shown. Section 3.9 shows the different behavior of ellipsoidal particles depending on the excentricity. Finally Section 3.10 shows the interaction of several particles connected to each other. In the following lengths are given in nanometers. The open circuit voltage corresponding to [61] is applied for the cathode material.

3.1. Spherical packing

The centers of the spheres are specified in Table A.5. Figure 3 shows the unit cell for the four different spherical packings.

Four different spherical packings are introduced, simple cubic (SC), body centered cubic (BCC), face centered cubic (FCC) and hexagonal close packed (HCP) [64]. The definition of a spherical packing entails the lengths of the unit cell, the radius of the spheres in the unit cells, and the centers of all spheres that have non-empty intersection with this unit cell. This gives an analytical description of the packing.

- SC: Unit cell $[0, 1] \times [0, 1] \times [0, 1]$. Radius $r = \frac{1}{2}$, 8 centers of spheres.
- BCC: Unit cell $[0, 1] \times [0, 1] \times [0, 1]$. Radius $r = \frac{\sqrt{3}}{4}$, 9 centers of spheres.
- FCC: Unit cell $[0, 1] \times [0, 1] \times [0, 1]$. Radius $r = \frac{\sqrt{2}}{4}$, 14 centers of spheres.
- HCP: Unit cell $[0, 1] \times [0, \sqrt{3}] \times [0, \sqrt{\frac{8}{3}}]$. Radius $r = \frac{1}{2}$, 14 centers of spheres.

The spherical packings are defined such that the spheres do not overlap. An elastic problem on such spherical packings is ill-posed for the contact points [65]. The numerical solution for the stress does not show uniform convergence for finer discretizations. The analytical solution to an elasticity problem posed in the presented manner possesses a singular value, such as infinitesimal small deformation and an infinite stress [66]. A numerical example is given to illustrate this behavior and to investigate the maximum stress occurring. Consider a cathode domain Ω_c consisting of two hemispheres with radius 50 in the domain $\Omega = (0, 100)^3$, see Figure 4.

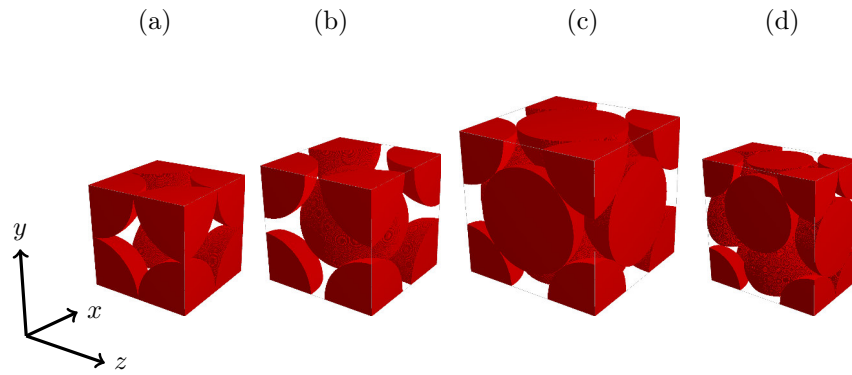


Figure 3: Unit cell of not regularised spherical packings. (a) SC. (b) BCC. (c) FCC. (d) HCP.

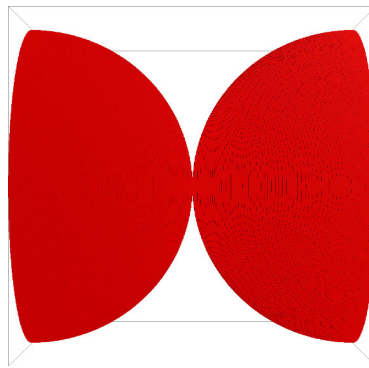


Figure 4: Microstructure for computation of elastic stresses

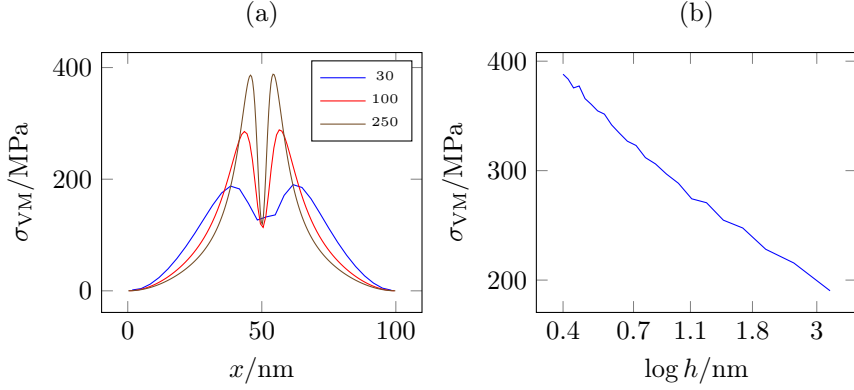


Figure 5: von Mises stress in a not regularised microstructure. (a) Along the line from M_1 to M_2 . (b) Maximum von Mises stress.

The centers of the two hemispheres are given as $\mathbf{M}_1 = (0, 50, 50)$ and $\mathbf{M}_2 = (100, 50, 50)$. The domain Ω_c is then defined as

$$\Omega_c = \{|\mathbf{x} - \mathbf{M}_1| < r \wedge |\mathbf{x} - \mathbf{M}_2| < r\}, \quad (31)$$

and $\Omega_e = \Omega \setminus \Omega_c$ is the electrolyte domain. A static elastic problem is considered and the concentration c inside the electrode material is set to the constant value $c(\mathbf{x}) = 0.5c_{\max}$. The elastic constants in cathode and electrolyte are chosen according to Table 2. Periodic boundary conditions are chosen in all three spatial dimensions. The spatial discretization with $N_1 = N_2 = N_3$ is chosen from $N_1 \in \{30, 40, \dots, 250\}$. Figure 5 (a) shows the resulting von Mises stress along the line from \mathbf{M}_1 to \mathbf{M}_2 . The solution for the von Mises stress does not converge. Figure 5 (b) shows the maximum von Mises stress. A limit value of the maximum von Mises stress cannot be extrapolated.

3.2. Geometric regularisation algorithms

In order to give a well-posed elastic problem, a geometric regularisation is introduced that enlarges the domain and gives a smooth surface of the domain Ω_c . Assume a pair of points $P = (\mathbf{M}_1, \mathbf{M}_2)$ that consists of two centers of spheres with the same radius R touching each other in a point. Therefore, it

holds $|\mathbf{M}_1 - \mathbf{M}_2| = 2R$. A local cylindric coordinate system is defined by projection onto (z, r) from the global coordinates $\mathbf{x} = (x_1, x_2, x_3)$. The third degree of freedom, the rotational angle around the center axis is neglected due to an assumption of axial symmetry for a geometric regularisation algorithm. The projection ψ is then given as

$$\psi : \begin{cases} \mathbb{R}^3 & \rightarrow \mathbb{R}^2, \\ \mathbf{x} & \mapsto \begin{pmatrix} z \\ r \end{pmatrix} = \begin{pmatrix} (\mathbf{x} - \mathbf{M}_1) \circ \frac{\mathbf{M}_1 - \mathbf{M}_2}{|\mathbf{M}_1 - \mathbf{M}_2|} \\ |(\mathbf{x} - \mathbf{M}_1) \times \frac{\mathbf{M}_1 - \mathbf{M}_2}{|\mathbf{M}_1 - \mathbf{M}_2|}| \end{pmatrix}. \end{cases} \quad (32)$$

This gives a projection from three-dimensional space into cylinder coordinates while disregarding the angle and assuming symmetry along this angle. That is why the coordinates are called z for the coordinate along the cylinder axis direction and r along the radial direction. A geometric regularisation function g is defined as

$$g : \begin{cases} \mathbb{R}^2 & \rightarrow \{0, 1\}, \\ \begin{pmatrix} z \\ r \end{pmatrix} & \mapsto f \begin{pmatrix} z \\ r \end{pmatrix}. \end{cases} \quad (33)$$

This function gives the value 0 to express that no coating is present at this point in space or 1 to express that coating material is present at this point in space. A regularisation domain is defined as a subset Ω_{coat} of the domain Ω_e and is given as

$$\Omega_{\text{coat}} = \{\mathbf{x} \in \Omega_e \mid f(\psi(\mathbf{x})) = 1\}. \quad (34)$$

An algorithm will be called regularisation if it possesses the following properties

- *Bounded regularisation:* $g(z, r) = 0$ if $(z, r) \notin [0, R] \times [0, 2R]$.

This restricts the regularisation to a reasonable domain around the contact point.

- *Axial symmetry:* $g(z, r) = g(2R - z, r)$ for all $(z, r) \in [0, R] \times [0, 2R]$.

This ensures that the regularisation is axially symmetric such that the

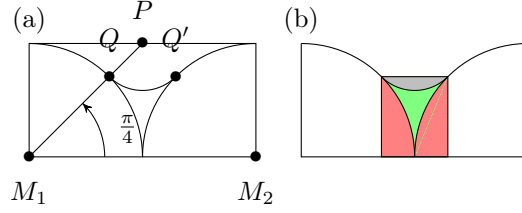


Figure 6: (a) Diagram for the derivation of the arc regularisation. (b) Diagram for the derivation of the volume fraction of the arc regularisation.

mapping from the set of center points to the ordered pairs $P = (M_1, M_2)$ is invariant to permutation.

- *Simply connected:* $\Omega_c \cup \Omega_{\text{coat}}$ is simply connected.

This reflects the basic property of a regularisation to be adhesive to the surface of the not regularised domain such that no holes are generated by the regularisation.

- *Smoothing:* The boundary of $\Omega_c \cup \Omega_{\text{coat}}$ is smooth.

This should prevent the divergent elastic solution as shown in Figure 5.

Next, two different regularisation functions are defined that fulfill the presented requirements. The analytic description of the regularisation function g is given as well as the volume fraction of the regularisation. The geometric derivations are supported by well-known formulas available in standard mathematical handbooks, e.g. in [67].

3.3. Arc regularisation

Figure 6 (a) depicts the projection domain $[0, 2R] \times [0, R]$.

The points M_1 , M_2 , P and Q have local coordinates $(0, 0)$, $(2R, 0)$, (R, R) and $(\frac{\sqrt{2}}{2}R, \frac{\sqrt{2}}{2}R)$ respectively. Additionally, values $z_l = \frac{\sqrt{2}}{2}R$ and $z_r = (2 - \frac{\sqrt{2}}{2})R$ are introduced, the r -coordinates of Q and Q' . A function $b(r, z) : [0, 2R] \times [0, R] \rightarrow \mathbb{R}$ is introduced as

$$b(r, z) = (z - R)^2 + (r - R)^2 - (\sqrt{2} - 1)^2 R^2. \quad (35)$$

The level set $\{b = 0\}$ includes the circle arc going through Q and Q' . The regularisation function is then

$$g(z, r) = \begin{cases} 0, & \text{if } z < z_l, \\ H(b(r, z)), & \text{if } z_l \leq z \leq z_r, \\ 0, & \text{if } z_r < z, \end{cases} \quad (36)$$

where H is the Heaviside function. This relates to the area under the circle which can then be calculated easily. Figure 6 (b) introduces colored domains for the derivation of the volume of the regularisation domain (green). The volume of the rotational body resulting from the gray segment is now calculated. Guldin's formula gives the volume of a rotational body as $V = 2\pi r_s A$, where A is the area of the rotating shape and r_s the distance of the centroid of it to the rotation axis. The area of a segment and a centroid are given as

$$\begin{aligned} A(\xi, q) &= \frac{q^2}{2} (2\xi - \sin(2\xi)) \\ d(\xi, q) &= \frac{4q \sin^3(\xi)}{3(2\xi - \sin(2\xi))}, \end{aligned} \quad (37)$$

where ξ is the angle and q is the radius of the segment [67]. The value of d gives the distance of the centroid from the radius. The values for angle and radius are $\xi = \frac{\pi}{4}$ and $q = (\sqrt{2} - 1)R$, respectively. The distance of the centroid to the rotational axis is then $r_s = R - d(\xi, q)$. The volume of a spherical cap (red in Figure 6) is $V_{\text{Cap}}(q, h) = \frac{\pi h^2}{3}(3q - h)$, where q is the radius and h is the height. Here, $q = r$ and $h = 1 - \cos(\frac{\pi}{4})$. The volume of a cylinder consisting of the colored parts in Figure 6 is $V_{\text{Cyl}} = \pi q^2 h$, where q is the radius and h is the height. Here, $h = 2 - 2\cos(\frac{\pi}{4})$ and $q = \sin(\frac{\pi}{4})$. The volume of the regularisation is then given as

$$\begin{aligned} V_R &= V_{\text{Cyl}} - V_{\text{Seg}} - 2V_{\text{Cap}} = \\ &= \frac{1}{2} (2\sqrt{2} - 3) (\pi - 4) \pi R^3 \\ &\approx 0.231346r^3 \end{aligned} \quad (38)$$

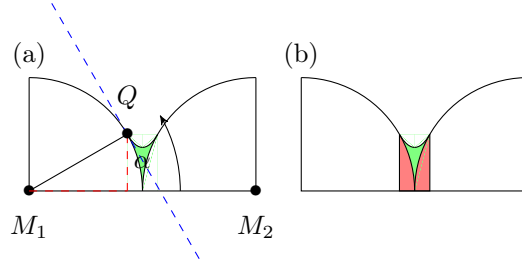


Figure 7: (a) Diagram for the derivation of the parabola regularisation. (b) Diagram for the derivation of the volume fraction of the parabola regularisation.

3.4. Parabola regularisation

Figure 7 depicts the projection domain $[0, 2R] \times [0, R]$. The point Q has coordinates $(R \cos(\alpha), R \sin(\alpha))$. Additionally, values $z_l = R \cos(\alpha)$ and $z_r = R(2 - \cos(\alpha))$ are introduced. The parabola is represented as the level set of the function $p(r, z) = a(z - x_s)^2 + b - r$, with $a, b, x_s \in \mathbb{R}$ being the parameters. Then $x_s = R$ due to axial symmetry of M_1 and M_2 . Furthermore,

$$R \cos(\alpha) = a(R \sin(\alpha) - R)^2 + b, \quad (39a)$$

$$-\cot(\alpha) = 2a(R \sin(\alpha) - R), \quad (39b)$$

where (39a) results from Q being on the parabola and (39b) results from the requirement that the slope is continuous at Q in order to get a C^1 -boundary. This gives

$$a = -\frac{\cot(\alpha)}{2(r \cos(\alpha) - r)}, \quad (40)$$

$$b = R \sin(\alpha) + \frac{1}{2}R \cot(\alpha)(\cos(\alpha) - 1).$$

The regularisation function is then

$$g(z, r) = \begin{cases} 0, & \text{if } z < z_l, \\ H(p(r, z)), & \text{if } z_l \leq z \leq z_r, \\ 0, & \text{if } z_r < z, \end{cases} \quad (41)$$

where H is the Heaviside function. Figure 6 (b) introduces colored domains for the derivation of the volume of the regularisation domain (green). The volume

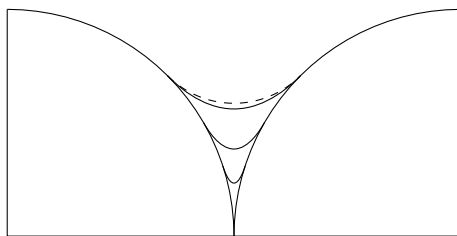


Figure 8: Comparison of arc and parabola regularisation for different angles α .

of the rotational body given by the parabola is given as an integral,

$$V_{\text{Para}} = \pi \int_{z_l}^{z_r} (a(x - x_s)^2 + b)^2 dx. \quad (42)$$

The volume of the spherical caps V_{Caps} is calculated as shown in the previous subsection. The volume of the regularisation is then given dependent on the angle α as

$$\begin{aligned} V_R(\alpha) &= V_{\text{Para}} - 2V_{\text{Cap}} = \\ &= \frac{16}{15} \pi \left(6 + 5 \cos(\alpha) + \cos(2\alpha) \csc(\alpha)^2 \sin\left(\frac{\alpha}{2}\right)^6 \right) r^3, \end{aligned} \quad (43)$$

$$V_R\left(\frac{\pi}{4}\right) \approx 0.20072r^3,$$

$$V_R\left(\frac{\pi}{6}\right) \approx 0.0436365r^3, \quad (44)$$

$$V_R\left(\frac{\pi}{10}\right) \approx 0.00594741r^3.$$

3.5. Comparison of regularisations

Figure 8 shows the arc regularisation and the parabola regularisation for $\alpha \in \{\frac{\pi}{4}, \frac{\pi}{6}, \frac{\pi}{10}\}$. With $\alpha = \frac{\pi}{4}$, the parabola regularisation uses the same analytic contact points as the arc regularisation but it has smaller volume fraction.

Figure 9 shows those four different regularisations in a 3D representation. In red the two hemispheres can be seen, the regularisation is shown in green.

Table 4 gives numerical values for the volume fraction of the different regularisations. Several spatial discretizations are realized with N being the number of nodes in direction x , y and z . This means the total number of finite volume

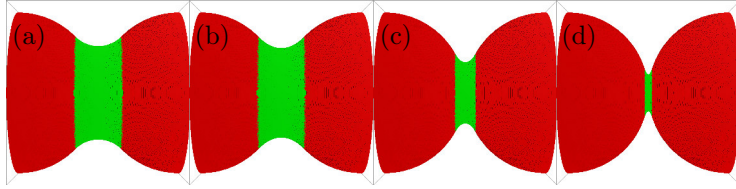


Figure 9: Regularisations of the elastic test microstructure. (a) Arc regularisation. (b)-(d) Parabola regularisation for different angles α .

Regularisation function	N=64	N=128	N=256	N=512	Analytical sol.
Arc	0.23096	0.23053	0.23151	0.23133	0.23135
Parabola, $\alpha = \frac{\pi}{4}$	0.19922	0.19913	0.20093	0.20072	0.2007
Parabola, $\alpha = \frac{\pi}{6}$	0.04248	0.04337	0.04364	0.04364	0.043637
Parabola, $\alpha = \frac{\pi}{10}$	0.00562	0.00568	0.00592	0.00593	0.0059474

Table 4: Volume fractions as parts of R^3

cells is N^3 . The result is compared to analytical limits. The volume of the sphere itself is in this case $\frac{4\pi}{3}R^3 \approx 4.19R^3$.

Figure 10 shows unit cells of regularised spherical packings.

3.6. Numerical test of the regularisation

The static elastic test example given before is repeated with a regularised domain. The parabola regularisation function is chosen with $\alpha = \frac{\pi}{6}$. The regularisation is added to the electrode material, $\Omega = \Omega_c \cup \Omega_{\text{coat}}$. All other parameters are set to the same values. Figure 11 (a) shows the resulting von Mises stress along the line from \mathbf{M}_1 to \mathbf{M}_2 . The solution converges numerically to a limit. Figure 11 (b) shows the maximum von Mises stress in the domain with respect to the spatial discretization width h . For the problem with the coated domain, the value for the maximum von Mises stress converges inside the domain. This numerical test is only done for coating and active material possessing the same linear-elastic material properties. It shows that the resulting regularisations are valid and define smooth surfaces of the microstructures.

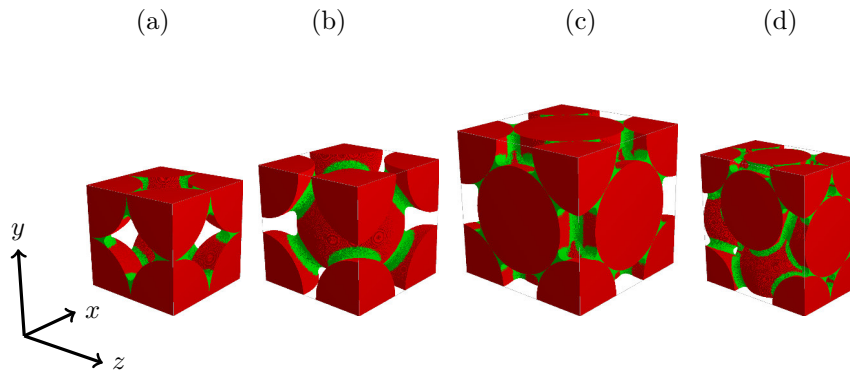


Figure 10: Unit cell of coated spherical packings. (a) SC. (b) BCC. (c) FCC. (d) HCP.

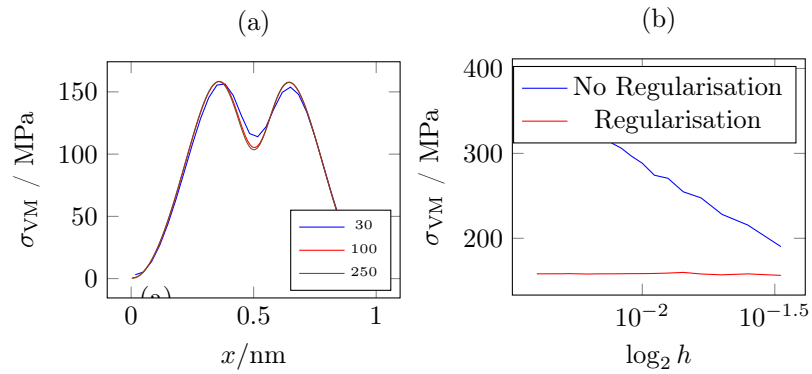


Figure 11: von Mises stress in a regularised microstructure. (a) Along the line from M_1 to M_2 . (b) Maximum von Mises stress.

In the following section, several numerical examples are shown. Basic mechanical effects are evaluated on structures with one and two spatial dimensions in Section 3.7. Next regular microstructures for cathode material such as ellipsoidal particles in Section 3.9 and multiple spherical particles in Section 3.10 are considered. As a reference a non-dimensional stress is used,

$$\sigma_0 = c_{\max}\theta E \approx 0.699\text{GPa} \Rightarrow \tilde{\sigma} = \frac{\sigma}{\sigma_0} \quad (45)$$

This allows the use of stress invariants as the von Mises stress and hydrostatic stress for the evaluation of different electrode particles and microstructures. The results can be translated to other material parameters.

3.7. Basic results with a beam structure for the cathode

A beam made from cathode material is considered with length $L_1 = 40$ nm and equal width and height $L_2 = L_3 = 1$ nm. It is charged with C-rate 1. The boundary value problem is then given by the electro-chemo-mechanical problem with the phase-field model in the cathode material. The boundary conditions are introduced in Equations 26 (C-rate 1), 27 and 29 (periodic mechanical boundary conditions). The initial conditions are given by a constant concentration corresponding to state of charge 0.01. The structure is charged from the right side ($x=40\text{nm}$). At the left side, the current collector resides and a no-flux boundary condition is applied. The spatial discretization is chosen as $N_1 = 100$ and $N_2 = N_3 = 1$ with $h = 1$ nm. Figure 12 (a) shows the lithium ion concentration in the cathode particle at SOC=0.5. Figure 12 (b) and (c) show magnifications of interesting regions. The lithium ion concentration is shown for different values for the partial molar volume θ . As θ increases, different effects can be seen. The equilibrium concentrations change. The low equilibrium concentration increases and vice versa. For $\theta = 0 \text{ cm}^3 \text{ mol}^{-1}$ they are $c_1 = 0.013c_{\max}$ and $c_2 = 0.987c_{\max}$, while for $\theta = 3 \text{ cm}^3 \text{ mol}^{-1}$ they are $c_1 \approx 0.1c_{\max}$ and $c_2 \approx 0.9c_{\max}$. A second effect is the widening of the interface width L . For $\theta = 0 \text{ cm}^3 \text{ mol}^{-1}$ it is $L = 3.3$ nm while for $\theta = 3 \text{ cm}^3 \text{ mol}^{-1}$ it is

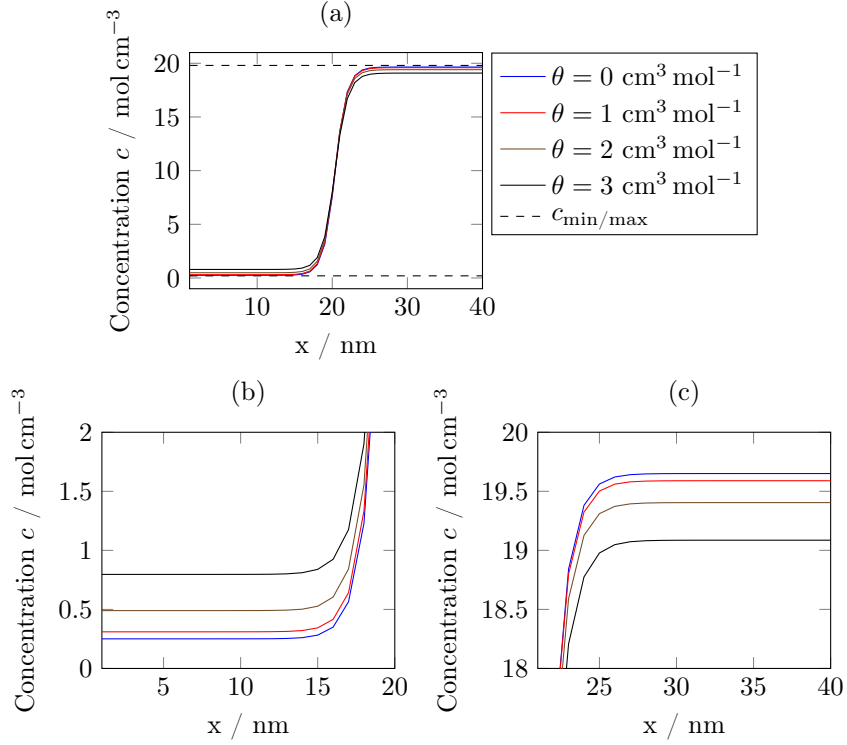


Figure 12: (a) Lithium ion concentration for different values of partial molar volume at state of charge 50%. (b)-(c) Magnifications of interesting regions.

$L \approx 4$ nm. Those results are well known but we still chose to include them as an introduction to the topic of phase separation.

Figure 13 (a) evaluates the hydrostatic stress for the exact same example at the state of charge 50%. It shows the hydrostatic stresses in the cathode particle. First, θ is chosen as $0 \text{ cm}^3 \text{mol}^{-1}$ and no stress occurs in the cathode material. For higher partial molar volumes, stress in both the lithium-rich phase and the lithium-depleted phase occurs. At the interface a smooth transition between the two stress states can be observed that also widens according to a widening interface. Figure 13 (b) shows the potential jump at the cathode-electrolyte interface. First, for higher values of θ the phase separation starts later and ends sooner. The phase-separated state is shorter compared to smaller values of θ .

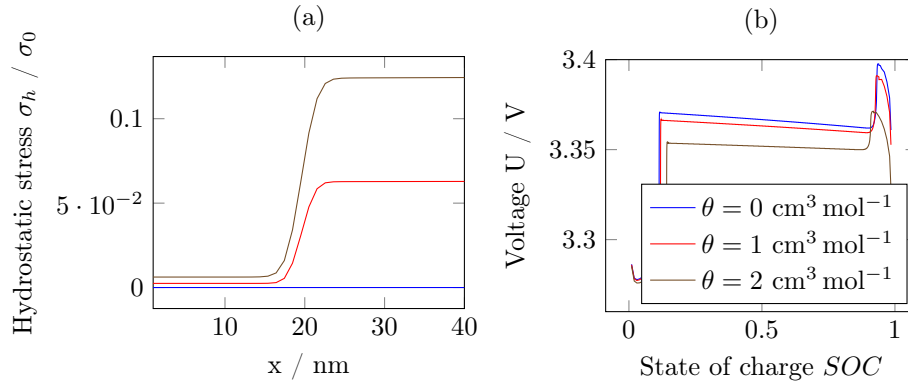


Figure 13: Hydrostatic stress and cell voltage for different values of partial molar volume. (a) Hydrostatic stress. (b) Cell voltage.

Second, for higher values of θ the electric potential during phase separation is lower. Although steps are occurring on the curves, numerical stability is given by the numerical method.

Figure 14 again relates to the example with a beam structure. It shows the cell voltage for different C-rates compared to the equilibrium voltage curve. It can be seen that the distance from the equilibrium curve increases for a larger C-rate as the overpotential η in (23) is larger. Also, the phase transition happens slightly later. Between states of charge 0.3 and 0.9 oscillations in the cell potential are observed. They are due to large time steps. Errors disappear for finer discretizations and the numerical solution can be adapted to the required accuracy as shown in previous works [25, 38].

3.8. Basic results with a spherical structure for the cathode

Now another example with another geometry for the microstructure. A spherical structure for the cathode is evaluated. Set $\Omega = (0, 100) \times (0, 60) \times (0, 60)$, $C = 1$, $N_1 = 100$ and $N_2 = N_3 = 60$. The cathode is a spherical particle with radius $r = 30 \text{ nm}$. Figure 15 shows the lithium ion concentration in the cathode particle at (a) $\text{SOC}=0.55$ and (b) $\text{SOC}=0.92$. The solution is rotationally symmetric and therefore a 2D projection is shown. At $\text{SOC}=0.55$

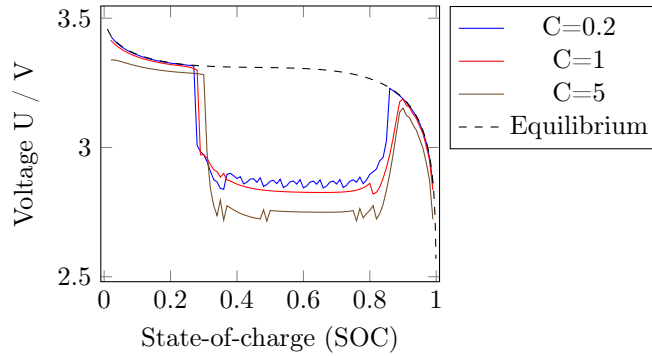


Figure 14: Electric potential for different C-rates. Compared to the open circuit potential in equilibrium state. The voltage drop is due to the high surface concentration during phase separation.

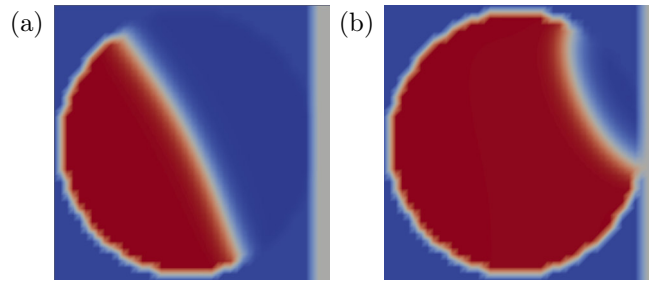


Figure 15: Lithium ion concentration for a cathode built of a spherical particle. (a) SOC=0.55. (b) SOC=0.92.

the particle is composed of approximately equally sized lithium-rich and lithium-depleted phase. Compare these results with Figure 3A in [2] where experimental measurements and the visualisation of a phase separation process in an electrode material are shown.

3.9.

3.10. Multiple spheres

In this examples, several spheres are combined to an electrode microstructure. The simulation domain is set to $\Omega = (0, 320) \times (0, 60) \times (0, 60)$, $N_1 = 320$ and $N_2 = N_3 = 60$. The parabola regularisation is applied between them. The

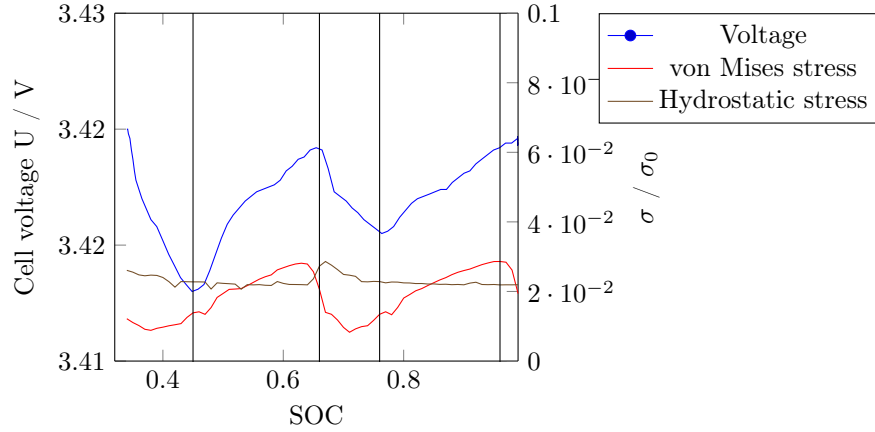


Figure 16: Cell voltage and stress invariants for a cathode built of multiple spherical particles. The concentration distribution at the times marked with vertical lines are shown in Figure 17.

spatial discretization width is $h = 1$ nm and the C-rate is 1. The boundary value problem is then given by the electro-chemo-mechanical problem with the phase-field model in the cathode material. The boundary conditions are introduced in Equations 26 (C-rate 1), 27 and 29. The initial conditions are given by a constant concentration corresponding to state of charge 0.01. Figure 16 shows the cell voltage as well as the maximum hydrostatic stress and the maximum von Mises stress. The plot is shown for SOC between 0.32 and 0.99 where phase separation is present. Both the hydrostatic stress and the cell voltage are to some extent periodic. Local minima for the cell voltage are attained for SOC=0.45 and SOC=0.76, a local maximum for SOC=0.66. The hydrostatic stress attains its maximum at SOC=0.96.

Figure 17 shows the lithium ion concentration in the structure at (a) SOC=0.45, (b) SOC=0.66, (c) SOC=0.76 and (d) SOC=0.96. (a) and (c) correspond to one or two completely filled particles, respectively, with small interfacial regions. This structure is analyzed for academic purposes to show the flexibility of the presented model. It is possible to demonstrate complex effects like the successive phase transition of different particles in a granular electrode. Although the small-strain model can be used to compute the high stresses occurring at



Figure 17: Lithium ion concentration for a cathode built of multiple spherical particles. (a)-(d) $\text{SOC} \in \{0.45, 0.66, 0.76, 0.96\}$, corresponding to the vertical lines in Figure 16.

the joint of different particles, in the presented way it can not be applied for the prediction of separation and fracture of the particles and the rearrangement following from this event.

The periodically rising stress in Figure 16 can be understood by and identified with the concentration distribution in Figure 17. By this method, it could be possible to understand and design electrode microstructures that minimize mechanical stresses. In the given example e.g., a high voltage for charging and a high von Mises stress appears when a particle is nearly filled and the phase interface is getting smaller, see $\text{SOC}=0.66\%$ and $\text{SOC}=0.96\%$.

4. Application on the micro-scale: Anode made of graphite

To give an example of application of the proposed method to realistic 3D data, in the present paper the microstructure of lithium-ion battery anodes is considered. A parametric stochastic 3D microstructure model has been developed and fitted to tomographic image data of the system of active particles in energy cell anodes in [40], see also [68] for power cell anodes and [69] for cathodes. Once calibrated to a given data set, stochastic microstructure models can be used to generate microstructures on the computer that are similar in a statistical sense to the data being modeled according to several morphological properties. Moreover, by systematic variation of model parameters it is possible to generate virtual, but realistic microstructures for materials that have not (yet) been manufactured in the laboratory. The combination of stochastic microstructure modeling with numerical simulations of functional properties allows us to identify preferable microstructures, a procedure called virtual materials testing.

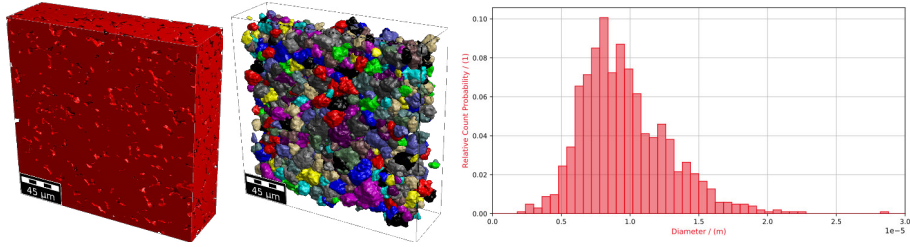


Figure 18: (i) Anode microstructure from tomography data. (ii) Reconstructed grains. (iii) Histogram of the equivalent diameters.

The model proposed in [40] has been validated with respect to electrochemical properties using spatially resolved simulations in [70]. In the present paper, a comparison of mechanical properties computed for tomographic image data and for realizations of the calibrated model is performed.

In this section, no phase-field model is applied, as graphite is not known for phase transition. Instead, a classic diffusion model derived from Fick’s law is applied as originally presented in [44].

4.1. Computer tomography data analysis

Tomography data from an anode microstructure is analyzed regarding the grain sizes and sphericities. A microstructure consisting of $400 \times 400 \times 119$ voxels with resolution $h = 0.438 \mu\text{m}$ is used, seen in Figure 18 (i). The watershed algorithm is applied and grains cut by the non periodic boundary are disregarded. Image artifacts resulting in grains smaller than $r_{\min} = 5 \mu\text{m}$ are disregarded, resulting in 1023 grains seen in Figure 18 (ii). The volume of each grain is used to calculate the diameter of a sphere with equal volume and the histogram of these equivalent diameters is given in Figure 18 (iii).

4.2. Virtual microstructure generation

The construction of the model is based on three main steps. To begin with, the sampling window is decomposed into a system of convex polytopes using a Laguerre tessellation, see Figure 19 (i). Later on, a particle will be placed in each polytope. However, to ensure complete connectivity of the system of

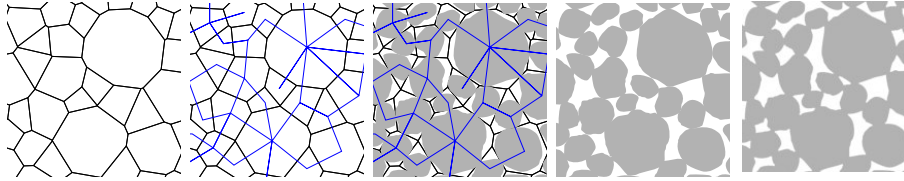


Figure 19: 2D sketch showing the individual steps of the stochastic microstructure model proposed in [40]. (i) Decomposition of the sampling window into convex polytopes. (ii) Construction of a connectivity graph. (iii) Modeling of particles according to the constraints given by the connectivity graph. (iv) The auxiliary tools are deleted. (v) A morphological closing is performed to mimic the effect of binder. Reprinted from [40], with permission from Elsevier.

particles, in the second step a connectivity graph is constructed, see the blue lines in Figure 19 (ii). This graph indicates which particles are supposed to be connected, i.e., if there is an edge of the graph between two polytopes, the corresponding particles will be forced to touch each other. This means that the particles radii along this edge are chosen as large as to ensure that the particle touch each other. In the third step, the particles themselves are modeled using spherical harmonic expansions of Gaussian random fields on the sphere. Thereby, the additional constraints that predefined points on the facets between those Laguerre polytopes where an edge of the connectivity graph is present are hit by the particles ensures that the particles touch each other as desired, see Figure 19 (iii). Then, the tessellation and connectivity graph are deleted, as they are only auxiliary tools for constructing the system of particles, see Figure 19 (iv). As a postprocessing step, a morphological closing is performed to mimic the effect of binder, see Figure 19 (v). A 3D comparison of tomographic image data and a corresponding model realization is shown in Figure 20.

4.3. Spherical symmetry

For validation of the method, a typical academic example as presented in other work [71, 72] is chosen. Figure 21 shows the lithium-ion concentration and corresponding stress invariants in an anode spherical particle with diameter 10 μm in radial direction during different states of charge. As the particle is

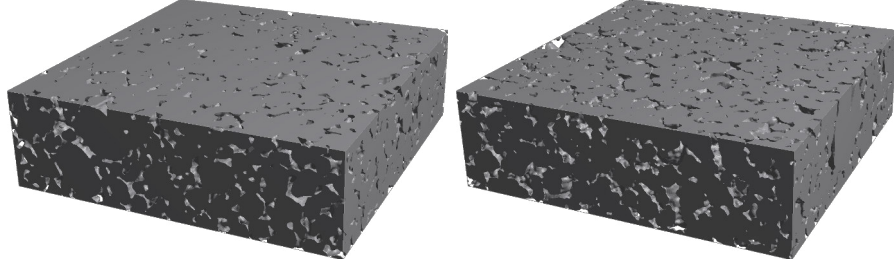


Figure 20: Left: CT image. Right: Simulated structure using the calibrated stochastic model.

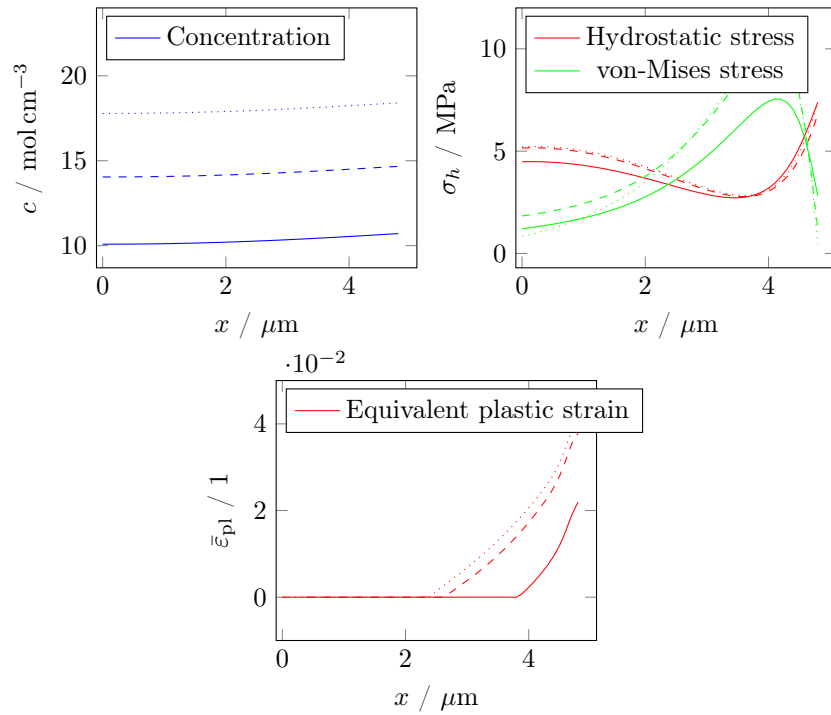


Figure 21: Radial-symmetric solution of (i) lithium-ion concentration and (ii) hydrostatic stress and von-Mises stress in a spherical particle for states of charge 40%, 55% (dashed) and 70% (dotted). (iii) Radial-symmetric solution of equivalent plastic strain in a spherical silicon particle for states of charge 21%, 23% and 25%.

spherical, no difference along tangential directions of the particle is observed and the properties only vary along the radial direction. The structure is a spherical particle in a cuboid domain. The spherical particle is either made of graphite for the linear-elastic simulation or silicon for the elasto-plastic simulation.

While the von-Mises stress maximum is situated in the outer shell of the particle, a local maximum of the hydrostatic stress is located in the center of the particle, compare to corresponding results in [73, 74, 72]. There, single particles with zero stress boundaries are discussed. Here, in the presented results, the increasing stress at the outer shell of the particle is due to the non zero stress boundaries. Appropriate models for the electrolyte as well as periodic mechanical boundary conditions are open for discussion. It is also possible to extend this example with an elastoplastic model. Given the model as presented in Section 2.5, the permanent change in the particle can be characterized by its equivalent plastic strain $\bar{\epsilon}_{pl}$. Figure 21 (iii) shows that the plastification immediately occurs during charging in the outer shell of the particle. For larger states of charge, the plastification increases in an growing outer shell of the particle.

4.4. *Virtually generated microstructures*

Figure 22 shows a comparison of the lithium-ion concentration and stress invariants in two different microstructures of anode material charged with C-rate 1 at 40% state of charge. In the top row, a tomographic image is depicted, while in the bottom row a realization of the calibrated stochastic microstructure model is shown. The electrode structure is charged from top to bottom. Concentration gradients arising from uneven interface current densities can be seen. The inner center of larger particles remains empty. Maxima of hydrostatic stress occur together with maxima of the lithium-ion concentration. Maxima of the von-Mises stress occur mainly at particle boundaries.

4.5. *Comparison between virtual and real microstructure simulations*

For a more thorough analysis, a total of 22 cutouts of tomographic image data and 20 simulated model realizations of the same size are chosen. These 42

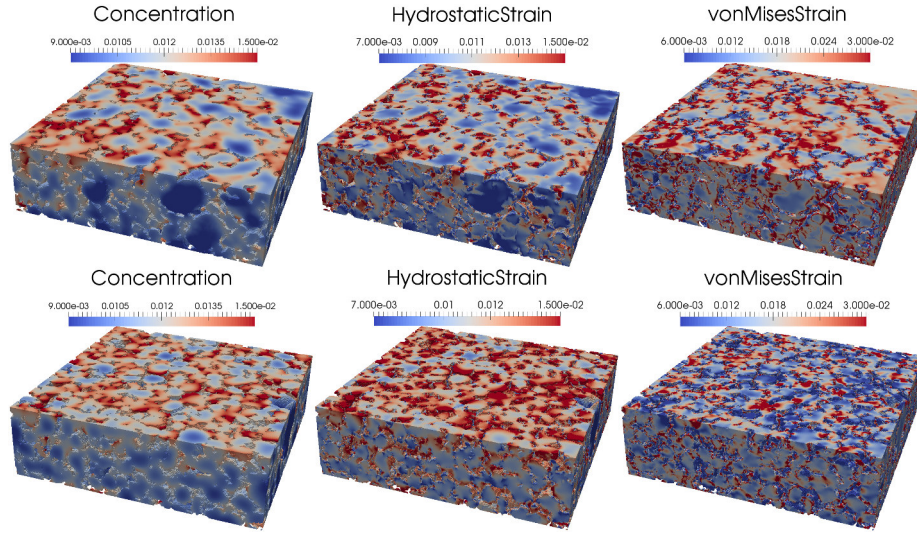


Figure 22: Full-field solution of lithium-ion concentration, hydrostatic stress and von-Mises stress in both tomographic (top) and simulated (bottom) microstructures.

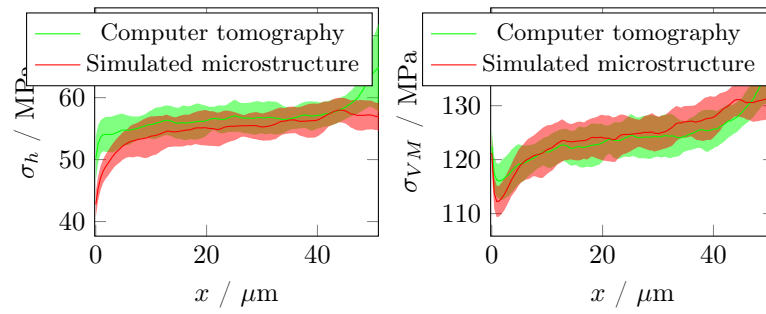


Figure 23: Comparison of the hydrostatic stress (left) and the von-Mises stress (right) for SOC=40% in the thickness direction. Plotted is the mean as well as ± 1 standard deviation.

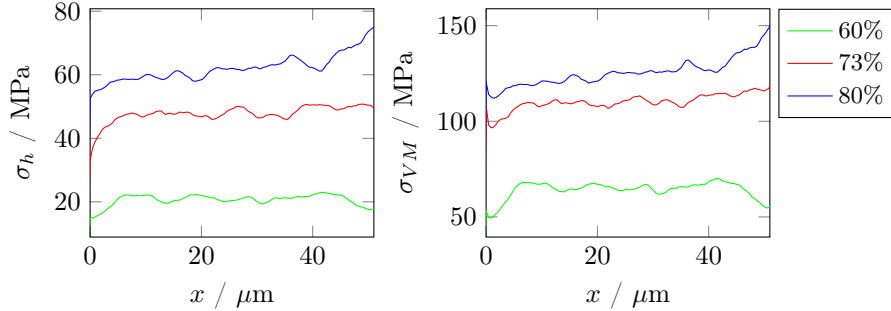


Figure 24: Comparison of the hydrostatic stress (left) and the von-Mises stress (right) for SOC=40% in the thickness direction. Plotted is the mean in each layer.

examples of anode microstructures are charged separately each with C-rate 1. The full-field solution gives numerical values for e.g. the hydrostatic stress at each finite volume center node. This is a three-dimensional field. This field is integrated in space along the y- and the z-direction and averaged. The result is a one-dimensional field. This field is the average hydrostatic stress in each layer. The procedure is done according to previous work in [70]. Then for both, tomographic image data and model realizations, the results are averaged and the mean and standard deviation are calculated. Figure 23 shows the resulting curves and ± 1 standard deviation. While boundary effects can be seen in both stress invariants, the deviations between the computer tomography solution and the stochastically generated structures are within the standard deviations. This shows that, except for the boundary of the structure, mechanical properties are in good agreement between real and simulated data. The differences at the boundary can be attributed to the fact that the solid volume fraction is larger on the boundary than in the center for tomographic image data, while this effect is not reproduced in the stochastic microstructure model.

Next, a set of three virtual microstructures is generated with varying solid volume fractions of 60%, 73% and 80% is generated using the method introduced in [41]. Again, each half-cell is charged with C-rate 1 and their full-field solution for both stress invariants averaged along second and third dimension. Figure 24

shows the resulting spatial trend. It can be seen that hydrostatic pressure as well as von-Mises stress are increasing with increasing solid volume fraction.

5. Conclusions

In this work the coupling of an electro-chemical model to a small-strain linear elasticity model is presented. The model is formulated with the help of variational derivatives and an approximation of the free energy functional. For the connection between different particles, different regularisation algorithms are introduced which ensure a Lipschitz boundary. In the numerical applications, several representative microstructures and particles are discussed. During phase separation into lithium-rich and lithium-depleted phase, high hydrostatic stresses occur that influence the equilibrium concentration of both phases. For ellipsoidal particles, the maximum stress inside during the charging varies highly. Regarding their excentricity, oblate particles are to be preferred due to their better ratio of surface to volume. For connected spheres the lithium-rich phase is shown to appear first in one particle and filling the structure one particle at a time. On the micro-scale, different structures are analyzed, which, e.g., allows for a comparison of mechanical properties between tomographic image data and simulated realizations of a stochastic microstructure model. Overall, a good agreement was found. Moreover, the approach allows us to investigate morphological advantages with respect to mechanical properties. Depending on material parameters the maximum C-rate and cycling effects can be evaluated. So far, the evaluation of maximum stress invariants inside the battery electrode particles allowed only for rough qualitative prediction of time and point of failure. In the future, additional damage or fracture models will allow for a more precise prediction of the aging under realistic load cases. In combination with stochastic microstructure modeling, a broad spectrum of virtual, but realistic microstructures can be analyzed accordingly, and morphologies with preferable mechanical properties can be identified by relating the maximum stresses occurring to properties such as the solid volume fraction.

Appendix A. Additional parameters

Table A.5 shows the numerical parameters for the generation of spherical packings. Given are the number of sphere centers required for the unit cell and the corresponding coordinates of each center. Many of these spheres contribute only with a small sector cut to the unit cell.

Packing	Number of centers	Center coordinates $M_i=(x_M, y_M, z_M)$
SC	8	$(0, 0, 0), (0, 0, 1), (0, 1, 0), (0, 1, 1),$ $(1, 0, 0), (1, 0, 1), (1, 1, 0), (1, 1, 1).$
BCC	9	$(0, 0, 0), (0, 0, 1), (0, 1, 0), (0, 1, 1),$ $(1, 0, 0), (1, 0, 1), (1, 1, 0), (1, 1, 1),$ $(\frac{1}{2}, \frac{1}{2}, \frac{1}{2}).$
FCC	14	$(0, 0, 0), (0, 0, 1), (0, 1, 0), (0, 1, 1),$ $(1, 0, 0), (1, 0, 1), (1, 1, 0), (1, 1, 1),$ $(\frac{1}{2}, \frac{1}{2}, 0), (\frac{1}{2}, \frac{1}{2}, 1), (\frac{1}{2}, 0, \frac{1}{2}),$ $(\frac{1}{2}, 1, \frac{1}{2}), (0, \frac{1}{2}, \frac{1}{2}), (1, \frac{1}{2}, \frac{1}{2}).$
HCP	14	$(0, 0, 0), (0, 0, \sqrt{\frac{8}{3}}), (0, \sqrt{3}, 0), (0, \sqrt{3}, \sqrt{\frac{8}{3}}),$ $(1, 0, 0), (1, 0, \sqrt{\frac{8}{3}}), (1, \sqrt{3}, 0), (1, \sqrt{3}, \sqrt{\frac{8}{3}}),$ $(\frac{1}{2}, \frac{\sqrt{3}}{2}, 0), (\frac{1}{2}, \frac{\sqrt{3}}{2}, \sqrt{\frac{8}{3}}), (\frac{1}{2}, \frac{\sqrt{3}}{6}, \sqrt{\frac{2}{3}}),$ $(\frac{1}{2}, \frac{7\sqrt{3}}{6}, \sqrt{\frac{2}{3}}), (0, \frac{2\sqrt{3}}{6}, \sqrt{\frac{2}{3}}), (1, \frac{2\sqrt{3}}{6}, \sqrt{\frac{2}{3}}).$

Table A.5: Parameters for the unit cells of spherical packings.

- [1] W. C. Chueh, F. E. Gabaly, J. D. Sugar, N. C. Bartelt, A. H. McDaniel, K. R. Fenton, K. R. Zavadil, T. Tyliczszak, W. Lai, K. F. McCarty, Intercalation pathway in many-particle LiFePO₄ electrode revealed by nanoscale state-of-charge mapping, Nano Letters 13 (3) (2013) 866–872 (feb 2013). doi:10.1021/nl3031899.
- [2] M. Ebner, F. Marone, M. Stampanoni, V. Wood, Visualization and quantification of electrochemical and mechanical degradation in Li ion batter-

- ies, *Science* 342 (6159) (2013) 716–720 (oct 2013). doi:10.1126/science.1241882.
- [3] Y. Zhu, J. W. Wang, Y. Liu, X. Liu, A. Kushima, Y. Liu, Y. Xu, S. X. Mao, J. Li, C. Wang, J. Y. Huang, In situ atomic-scale imaging of phase boundary migration in FePO₄ microparticles during electrochemical lithiation, *Advanced Materials* 25 (38) (2013) 5461–5466 (jul 2013). doi:10.1002/adma.201301374.
- [4] Y. Li, H. G. Lee, B. Xia, J. Kim, A compact fourth-order finite difference scheme for the three-dimensional Cahn-Hilliard equation, *Computer Physics Communications* 200 (2016) 108–116 (2016). doi:10.1016/j.cpc.2015.11.006.
- [5] C. Andersson, Phase-field simulation of dendritic solidification, Ph.D. thesis, Royal Institute of Technology Stockholm (2002).
- [6] I. Harari, J. Dolbow, Analysis of an efficient finite element method for embedded interface problems, *Computational Mechanics* 46 (2010) 205–211 (2010). doi:10.1007/s00466-009-0457-5.
- [7] S. Mitchell, M. Vynnycky, Finite-difference methods with increased accuracy and correct initialization for one-dimensional stefan problems, *Applied Mathematics and Computation* 215 (4) (2009) 1609–1621 (2009). doi:10.1016/j.amc.2009.07.054.
- [8] J. E. Cahn, J. W. Hilliard, Free energy of a nonuniform system. I. Interfacial free energy, *The Journal of Chemical Physics* 28 (2) (1958) 258–267 (1958). arXiv:9809069v1, doi:10.1063/1.1744102.
- [9] C. Kuhn, R. Müller, A phase field model for fracture, *Proceedings in Applied Mathematics and Mechanics* 8 (1) (2008) 10223–10224 (2008). doi:10.1002/pamm.200810223.
- [10] R. Müller, D. Gross, D. Schrade, B. X. Xu, Phase field simulation of domain structures in ferroelectric materials within the context of inhomogene-

- ity evolution, *International Journal of Fracture* 147 (1-4) (2007) 173–180 (2007). doi:10.1007/s10704-007-9153-7.
- [11] R. Müller, A phase field model for the evolution of martensite microstructures in metastable austenites, Ph.D. thesis, TU Kaiserslautern (2016).
- [12] C. Kuhn, Numerical and analytical investigation of a phase field model for fracture, Ph.D. thesis, Technical University Darmstadt (2013).
- [13] C. Plate, Fracture Mechanical Analysis of Failure Processes in Antarctic Ice Shelves, Ph.D. thesis, TU Kaiserslautern (2015).
- [14] G. K. Singh, G. Ceder, M. Z. Bazant, Intercalation dynamics in rechargeable battery materials: General theory and phase-transformation waves in LiFePO_4 , *Electrochimica Acta* 53 (26) (2008) 7599–7613 (2008). doi:10.1016/j.electacta.2008.03.083.
- [15] D. Burch, Intercalation Dynamics in Lithium-ion Batteries, Ph.D. thesis, Massachusetts Institute of Technology, Cambridge (2009).
- [16] M. Z. Bazant, Theory of chemical kinetics and charge transfer based on nonequilibrium thermodynamics., *Accounts of Chemical Research* 46 (5) (2013) 1144–1160 (2013). doi:10.1021/ar300145c.
- [17] A. Abdellahi, O. Akyildiz, R. Malik, K. Thornton, G. Ceder, The thermodynamic stability of intermediate solid solutions in LiFePO_4 nanoparticles, *Journal of Materials Chemistry A* 4 (15) (2016) 5436–5447 (2016). doi:10.1039/c5ta10498j.
- [18] T. Hofmann, Phase-field methods for deformation processes in lithium-ion batteries, Ph.D. thesis, TU Kaiserslautern (2018).
- [19] Y. Zeng, M. Z. Bazant, Phase separation dynamics in isotropic ion-intercalation particles, *SIAM Journal on Applied Mathematics* 74 (4) (2013) 980–1004 (2013). arXiv:1309.4543, doi:10.1137/090750688.

- [20] M. J. Welland, D. Karpeyev, D. T. O'Connor, O. Heinonen, Miscibility gap closure, interface morphology, and phase microstructure of 3D Li_xFePO_4 nanoparticles from surface wetting and coherency strain, *ACS Nano* 9 (10) (2015) 9757–9771 (sep 2015). doi:10.1021/acs.nano.5b02555.
- [21] M. Huttin, Phase-field modeling of the influence of mechanical stresses on charging and discharging processes in lithium ion batteries, Ph.D. thesis, Karlsruhe Institute of Technology (2014).
- [22] C. V. D. Leo, E. Rejovitzky, L. Anand, A Cahn-Hilliard-type phase-field theory for species diffusion coupled with large elastic deformations: Application to phase-separating li-ion electrode materials, *Journal of the Mechanics and Physics of Solids* 70 (2014) 1–29 (2014). doi:10.1016/j.jmps.2014.05.001.
- [23] M. Tang, J. F. Belak, M. R. Dorr, Anisotropic phase boundary morphology in nanoscale olivine electrode particles, *The Journal of Physical Chemistry C* (2011) 4922–4926 (2011).
- [24] D. A. Cogswell, M. Z. Bazant, Theory of coherent nucleation in phase-separating nanoparticles, *Nano Letters* 13 (2013) 7–12 (2013). doi:10.1021/nl400497t.
- [25] T. Hofmann, R. Müller, H. Andrä, J. Zausch, Numerical simulation of phase separation in cathode materials of lithium ion batteries, *International Journal of Solids and Structures* 100-101 (2016) 456–469 (2016). doi:10.1016/j.ijsolstr.2016.09.018.
- [26] W. Dreyer, J. Jamnik, C. Gohlke, R. Huth, J. Moškon, M. Gaberšček, The thermodynamic origin of hysteresis in insertion batteries, *Nature Materials* 9 (5) (2010) 448–453 (apr 2010). doi:10.1038/nmat2730.
- [27] T. R. Ferguson, M. Z. Bazant, Nonequilibrium thermodynamics of porous electrodes, *Journal of The Electrochemical Society* 159 (12) (2012) A1967–A1985 (2012). arXiv:1204.2934, doi:10.1149/2.048212jes.

- [28] T. R. Ferguson, M. Z. Bazant, Phase transformation dynamics in porous battery electrodes, *Electrochimica Acta* 146 (2014) 89–97 (2014). doi:10.1016/j.electacta.2014.08.083.
- [29] Y. Li, F. E. Gabaly, T. R. Ferguson, R. B. Smith, N. C. Bartelt, J. D. Sugar, K. R. Fenton, D. A. Cogswell, A. L. D. Kilcoyne, T. Tyliszczak, M. Z. Bazant, W. C. Chueh, Current-induced transition from particle-by-particle to concurrent intercalation in phase-separating battery electrodes, *Nature Materials* 13 (12) (2014) 1149–1156 (sep 2014). doi:10.1038/nmat4084.
- [30] B. Orvananos, T. R. Ferguson, H.-C. Yu, M. Z. Bazant, K. Thornton, Particle-level modeling of the charge-discharge behavior of nanoparticulate phase-separating Li-ion battery electrodes, *Journal of The Electrochemical Society* 161 (4) (2014) A535–A546 (2014). doi:10.1149/2.024404jes.
- [31] V. Taralova, Upscaling approaches for nonlinear processes in lithium-ion batteries, Ph.D. thesis, TU Kaiserslautern (2015).
- [32] S. N. Chiu, D. Stoyan, W. S. Kendall, J. Mecke, *Stochastic Geometry and Its Applications*, J. Wiley & Sons, Chichester, 2013 (2013).
- [33] O. Stenzel, L. J. A. Koster, R. Thiedmann, S. D. Oosterhout, R. A. J. Janssen, V. Schmidt, A new approach to model-based simulation of disordered polymer blend solar cells, *Advanced Functional Materials* 22 (6) (2012) 1236–1244 (2012). doi:10.1002/adfm.201102095.
- [34] D. Westhoff, J. Skibinski, O. Šedivý, B. Wysocki, T. Wejrzanowski, V. Schmidt, Investigation of the relationship between morphology and permeability for open-cell foams using virtual materials testing, *Materials & Design* 147 (2018) 1–10 (2018). doi:10.1016/j.matdes.2018.03.022.
- [35] M. Neumann, J. Staněk, O. M. Pecho, L. Holzer, V. Beneš, V. Schmidt, Stochastic 3D modeling of complex three-phase microstructures in SOFC-electrodes with completely connected phases, *Computational Materials Sci-*

- ence 118 (2016) 353–364 (2016). doi:10.1016/j.commatsci.2016.03.013.
- [36] O. Stenzel, D. Westhoff, I. Manke, M. Kasper, D. P. Kroese, V. Schmidt, Graph-based simulated annealing: a hybrid approach to stochastic modeling of complex microstructures, *Modelling and Simulation in Materials Science and Engineering* 21 (5) (2013) 055004 (2013). doi:10.1088/0965-0393/21/5/055004.
- [37] O. Stenzel, O. Pecho, L. Holzer, M. Neumann, V. Schmidt, Big data for microstructure-property relationships: A case study of predicting effective conductivities, *AIChE Journal* 63 (9) (2017) 4224–4232 (2017). doi:10.1002/aic.15757.
- [38] T. Hofmann, R. Müller, H. Andrä, A fast immersed interface method for the Cahn-Hilliard equation with arbitrary boundary conditions in complex domains, *Computational Materials Science* 140 (2017) 22–31 (2017). doi:https://doi.org/10.1016/j.commatsci.2017.08.025.
- [39] T. Hofmann, D. Westhoff, J. Feinauer, H. Andrä, J. Zausch, V. Schmidt, R. Müller, Electro-chemo-mechanical simulation of 3D microstructures for lithium-ion batteries, *Proceedings of the 6th European Conference on Computational Mechanics, Glasgow 6* (2018) , In Press (2018).
- [40] J. Feinauer, T. Brereton, A. Spetl, M. Weber, I. Manke, V. Schmidt, Stochastic 3D modeling of the microstructure of lithium-ion battery anodes via gaussian random fields on the sphere, *Computational Materials Science* 109 (2015) 137–146 (2015). doi:10.1016/j.commatsci.2015.06.025.
- [41] D. Westhoff, I. Manke, V. Schmidt, Generation of virtual lithium-ion battery electrode microstructures based on spatial stochastic modeling, *Computational Materials Science* 151 (2018) 53–64 (2018). doi:10.1016/j.commatsci.2018.04.060.

- [42] Y. Zeng, P. Albertus, R. Klein, N. Chaturvedi, A. Kojic, M. Z. Bazant, J. Christensen, Efficient conservative numerical schemes for 1d nonlinear spherical diffusion equations with applications in battery modeling, *Journal of The Electrochemical Society* 160 (9) (2013) A1565–A1571 (2013). doi: 10.1149/2.102309jes.
- [43] X. Zhang, W. Shyy, A. M. Sastry, Erratum: Numerical simulation of intercalation-induced stress in Li-ion battery electrode particles, *Journal of The Electrochemical Society* 154 (12) (2007) S21 (2007). doi: 10.1149/1.2793718.
- [44] A. Latz, J. Zausch, Thermodynamic consistent transport theory of li-ion batteries, *Journal of Power Sources* 196 (6) (2011) 3296–3302 (2011). doi: 10.1016/j.jpowsour.2010.11.088.
- [45] S. Hein, A. Latz, Influence of local lithium metal deposition in 3D microstructures on local and global behavior of lithium-ion batteries, *Electrochimica Acta* 201 (2015) 354–365 (2015). doi:10.1016/j.electacta.2016.01.220.
- [46] Y. Qi, L. G. Hector, C. James, K. J. Kim, Lithium concentration dependent elastic properties of battery electrode materials from first principles calculations, *Journal of The Electrochemical Society* 161 (11) (2014) F3010–F3018 (2014). doi:10.1149/2.0031411jes.
URL <https://doi.org/10.1149/2.0031411jes>
- [47] K. Zhao, W. L. Wang, J. Gregoire, M. Pharr, Z. Suo, J. J. Vlassak, E. Kaxiras, Lithium-assisted plastic deformation of silicon electrodes in lithium-ion batteries: a first-principles theoretical study, *Nano Letters* 11 (7) (2011) 2962–2967 (2011). doi:10.1021/nl201501s.
- [48] C. V. D. Leo, E. Rejovitzky, L. Anand, Diffusion–deformation theory for amorphous silicon anodes: The role of plastic deformation on electrochemical performance, *International Journal of Solids and Structures* 67-68 (2015) 283–296 (2015). doi:10.1016/j.ijsolstr.2015.04.028.

- [49] N. Provatas, K. Elder, Phase-Field Methods in Materials Science and Engineering, Wiley-VCH, 2010 (2010).
- [50] K. Zhao, M. Pharr, J. J. Vlassak, Z. Suo, Fracture of electrodes in lithium-ion batteries caused by fast charging, *Journal of Applied Physics* 108 (7) (2010) 073517 (2010). doi:10.1063/1.3492617.
- [51] A. F. Bower, P. R. Guduru, A simple finite element model of diffusion, finite deformation, plasticity and fracture in lithium ion insertion electrode materials, *Modelling and Simulation in Materials Science and Engineering* 20 (4) (2012) 045004 (2012). doi:10.1088/0965-0393/20/4/045004.
- [52] L. Brassart, K. Zhao, Z. Suo, Cyclic plasticity and shakedown in high-capacity electrodes of lithium-ion batteries, *International Journal of Solids and Structures* 50 (7-8) (2013) 1120–1129 (2013). doi:10.1016/j.ijsolstr.2012.12.019.
- [53] H. Dal, C. Miehe, Computational electro-chemo-mechanics of lithium-ion battery electrodes at finite strains, *Computational Mechanics* 55 (2) (2014) 303–325 (dec 2014). doi:10.1007/s00466-014-1102-5.
- [54] J. Simo, T. Hughes, *Computational Inelasticity*, Springer, New York, 2000 (2000).
- [55] J. Spahn, An efficient multiscale method for modeling progressive damage in composite materials, Ph.D. thesis, TU Kaiserslautern (2015).
- [56] R. S. Nejad, A Parallel Elastic and Inelastic Heterogeneous Multiscale Method for Rate-independent Materials, Ph.D. thesis, Karlsruhe Institute of Technology (2017).
- [57] D. Noren, M. Hoffman, Clarifying the butler–volmer equation and related approximations for calculating activation losses in solid oxide fuel cell models, *Journal of Power Sources* 152 (2005) 175–181 (dec 2005). doi:10.1016/j.jpowsour.2005.03.174.
URL <https://doi.org/10.1016/j.jpowsour.2005.03.174>

- [58] K. Oldham, J. Myland, *Fundamentals of Electrochemical Science*, Academic Press, 2012 (2012).
- [59] S. Rangarajan, V. Yegnanarayanan, M. Muthukumar, Current losses in a bipolar cell — II: An analysis of the butler–volmer regime, *Electrochimica Acta* 44 (2-3) (1998) 491–502 (sep 1998). doi:10.1016/s0013-4686(98)00002-4.
URL [https://doi.org/10.1016/s0013-4686\(98\)00002-4](https://doi.org/10.1016/s0013-4686(98)00002-4)
- [60] P. Vijay, M. O. Tadé, Improved approximation for the butler-volmer equation in fuel cell modelling, *Computers & Chemical Engineering* 102 (2017) 2–10 (jul 2017). doi:10.1016/j.compchemeng.2016.10.018.
URL <https://doi.org/10.1016/j.compchemeng.2016.10.018>
- [61] C. Zhang, J. Jiang, L. Zhang, S. Liu, L. Wang, P. Loh, A generalized SOC-OCV model for lithium-ion batteries and the SOC estimation for LNMCO battery, *Energies* 9 (11) (2016) 900 (2016). doi:10.3390/en9110900.
- [62] K. G. Gallagher, D. W. Dees, A. N. Jansen, D. P. Abraham, S.-H. Kang, A volume averaged approach to the numerical modeling of phase-transition intercalation electrodes presented for Li_xC_6 , *Journal of The Electrochemical Society* 159 (12) (2012) A2029–A2037 (2012). doi:10.1149/2.015301jes.
URL <https://doi.org/10.1149/2.015301jes>
- [63] B. Lu, Y. Song, Q. Zhang, J. Pan, Y.-T. Cheng, J. Zhang, Voltage hysteresis of lithium ion batteries caused by mechanical stress, *Physical Chemistry Chemical Physics* 18 (6) (2016) 4721–4727 (2016). doi:10.1039/c5cp06179b.
URL <https://doi.org/10.1039/c5cp06179b>
- [64] A. B. Ellis, M. J. Geselbracht, B. J. Johnson, *Teaching General Chemistry: A Materials Science Companion*, An American Chemical Society Publication, Washington, 1993 (1993).

- [65] A. K. Rao, Stress concentrations and singularities at interface corners, ZAMM - Zeitschrift für Angewandte Mathematik und Mechanik 51 (5) (1971) 395–406 (1971). doi:10.1002/zamm.19710510509.
- [66] M. L. Williams, Stress singularities resulting from various boundary conditions in angular corners of plates in extension, Journal of Applied Mechanics 19 (4) (1952) 526–528 (1952).
- [67] N. Bronstein, A. Semendjajew, Taschenbuch der Mathematik, Europa-Lehrmittel, Haan-Gruiten, 2016 (2016).
- [68] D. Westhoff, J. Feinauer, K. Kuchler, T. Mitsch, I. Manke, S. Hein, A. Latz, V. Schmidt, Parametric stochastic 3D model for the microstructure of anodes in lithium-ion power cells, Computational Materials Science 126 (2017) 453–467 (2017). doi:10.1016/j.commatsci.2016.09.006.
- [69] K. Kuchler, D. Westhoff, J. Feinauer, T. Mitsch, I. Manke, V. Schmidt, Stochastic model for the 3D microstructure of pristine and cyclically aged cathodes in Li-ion batteries, Modelling and Simulation in Materials Science and Engineering 26 (3) (2018) 035005 (2018). doi:10.1088/1361-651x/aaa6da.
- [70] S. Hein, J. Feinauer, D. Westhoff, I. Manke, V. Schmidt, A. Latz, Stochastic microstructure modeling and electrochemical simulation of lithium-ion cell anodes in 3D, Journal of Power Sources 336 (2016) 161–171 (2016). doi:10.1016/j.jpowsour.2016.10.057.
- [71] V. Malavé, J. R. Berger, H. Zhu, R. J. Kee, A computational model of the mechanical behavior within reconstructed Li_xCoO_2 Li-ion battery cathode particles, Electrochimica Acta 130 (2014) 707–717 (2014). doi:10.1016/j.electacta.2014.03.113.
- [72] M. Klinsmann, D. Rosato, M. Kamlah, R. M. McMeeking, Modeling crack growth during Li insertion in storage particles using a fracture phase field

approach, *Journal of the Mechanics and Physics of Solids* 92 (2016) 313–344 (2016). doi:10.1016/j.jmps.2016.04.004.

[73] M. Huttin, M. Kamlah, Phase-field modeling of stress generation in electrode particles of lithium ion batteries, *Applied Physics Letters* 101 (13) (2012) 133902 (2012). doi:10.1063/1.4754705.

[74] P. Stein, B. Xu, 3D isogeometric analysis of intercalation-induced stresses in Li-ion battery electrode particles, *Computer Methods in Applied Mechanics and Engineering* 268 (2014) 225–244 (2014). doi:10.1016/j.cma.2013.09.011.